

Structural Characterization and Room Temperature Low-Frequency Raman Scattering from MAPbI₃ Halide Perovskite Films Rigidized by Cesium Incorporation

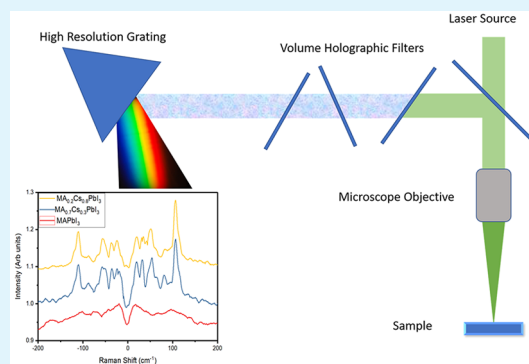
Vinayaka H. Damle,[†] Laxman Gouda,[†] Shay Tirosh, and Yaakov R. Tischler*[‡]

Department of Chemistry, Institute for Nanotechnology & Advanced Materials, Bar-Ilan University, Ramat Gan 5290000, Israel

Supporting Information

ABSTRACT: The structural instability of organometal halide perovskites (OHP) is one of the major issues concerning commercialization of perovskite solar cells. Probing this intrinsic instability is one of the major milestones and challenging tasks toward enhancing the lifespan of the material. Here we have incorporated Cs ions into methylammonium lead iodide (MAPbI₃) films and studied the thin film structural and optical properties. Incorporation of Cs into MAPbI₃ leads to formation of both α -CsPbI₃ and δ -CsPbI₃ phases, black and yellow, respectively, as indicated by the evolution of the optical band edge and X-ray diffraction (XRD) spectrum. At a concentration of 20% Cs ions, we observe the existence of a stable α -CsPbI₃ phase. Incorporating 59% or more Cs ions yields the yellow phase of CsPbI₃, due to alloying of Cs with the MAPbI₃ matrix. The structural transformations observed in absorption spectra and XRD are confirmed by low-frequency Raman spectroscopy. The thermally induced structural fluctuations in pure MAPbI₃ films are damped upon Cs incorporation, thus bringing long-range stabilized order to the perovskite structure and enabling for the first time observation of low-frequency Raman scattering at room temperature for OHPs. In addition to this, Cs incorporation rigidizes the perovskite film and sharpens all low-frequency vibrational peaks. This rigidizing effect can explain the importance of incorporating and alloying heavy elements into OHPs to bring both chemical stability and photostability.

KEYWORDS: low frequency Raman, cesium incorporation, hybrid perovskite, phonon damping, perovskite stability



Organometal halide perovskite (OHP) materials are extensively studied and have become game-changing materials with photovoltaic properties. The solar cell efficiencies of perovskite sensitized solar cells (PSSC) are reported for >23%, which is close to theoretical efficiency limit of the solar cells.¹ Ease of chemical synthesis and broad and high absorption coefficient $\alpha > 10^5 \text{ cm}^{-1}$, with tunable bandgap of 1.5–2.5 eV, make these materials even more interesting for PV applications.² The OHPs are also considered as fitting semiconductor materials with reference to their electrical conductivity, balanced long-range carrier diffusion length, high carrier mobility, and longer carrier lifetime.³ This class of materials is an excellent low-temperature solution processed low-cost semiconductor with very low defect density.⁴ OHPs are a special class of semiconductors as they possess both ionic and electronic carrier transport under electrical bias. Application of solvent engineering and variation of chemical composition enable facile tunability of absorption and emission band position and widths. This tunability has led to further scientific investigations, yielding different photonic properties and applications such as photodetectors, LEDs, and lasers.⁵

OHP based solar cells are of great interest for the scientific and industrial research community. However, a central issue with them is their low chemical stability and photostability, resulting in high susceptibility toward chemical and structural

degradation in the presence of moisture and light, respectively.⁵ The degradation of the perovskite structure is through a mechanism that favors PbI₂ formation, and therefore, stabilizing perovskites has been the primary interest. Several chemical approaches have been tried and found to be promising in preventing moisture induced degradation; however, photoinduced instability is still a challenge.⁶ It is accepted that kinetic phenomena in the perovskites such as ion migration, defect migration, and photoinduced reversible structural deformation are causing the instability.⁷

The mixed cation approach in perovskite fabrication is a promising method for enhancement of both photostability and performance in OHPs.⁸ For example, incorporating cesium into halide perovskites makes the structure more rigid, resulting in increased chemical and thermal stability;⁹ this observation is supported more recently by first principle calculations.¹⁰ The composition engineering of Br, I, Sn, Pb, Rb, Cs, formamidinium (FA), and methylammonium (MA) is reported to yield the highest OHP photovoltaic (PV) performance thus far with considerable increase in stability.

Received: September 13, 2018

Accepted: December 10, 2018

Published: December 10, 2018

The performance of mixed cation solar cells depends on both the composition and phase of the perovskite structure, with the tetragonal phase maintaining higher efficiency.² It has been observed that Cs cation incorporation alone is sufficient to bring photostability and to passivate recombination sites and trap states;^{10,11} however, a detailed explanation has not yet been given. It is observed that Cs incorporation changes the properties of the perovskite cage system. An additional open question is why mixed cationic hybrid structures yield enhancements in photostability and why alloying Cs influences photostability more than mere incorporation of Cs into the MAPbI₃ matrix.

In this study, we report Raman spectroscopy and low-frequency Raman spectroscopy (LFRS) to elucidate Cs incorporation into the MAPbI₃ hybrid perovskite structure. We have performed an MA to Cs cation exchange reaction on an MAPbI₃ neat film and characterized the OHP structure for Cs/MA composition ratio, mainly focusing on the influence that incorporating Cs has on the structure and rigidity of OHPs, and the evolution of optical properties, in particular absorption and PL spectra, with structural changes.

MAPbI₃ possesses a nonrigid tetragonal lattice crystal, where the methylamine ion interacts with the PbI₂ cage with weak van der Waals force, resulting in continuous flipping of the dipole due to molecular and lattice vibration. The Pb–I bonds in this hybrid perovskite structure are highly strained, with the size of the cation altering the size of the lattice and the Pb–I bond strength.¹² The electronic band structure in hybrid perovskite is mainly derived from the p-orbitals of Pb and I bonds. Thus, the alteration of bond length and strength of the Pb–I bonds give bandgap tunability, which is experimentally demonstrated by changing the composition of halide (I, Br, Cl) and cations (MA, FA, Cs, Rb).¹³ The changes in the composition also favors the other stable crystal phases, such as orthorhombic, tetragonal, and cubic structure, but with respect to geometry and composition, some of them are non-photovoltaic which are of less technological interest.⁷

With the main focus on understanding Cs incorporation induced stability, standalone films of MAPbI₃ were subjected to Cs⁺ incorporation by dipping into CsI solution. Thermodynamic minimization of strained tetragonal structure and affinity toward a smaller cation together favor controlled exchange of MA⁺ ion in the film with the Cs⁺ ion in the solution; subsequently, the entire MA⁺ ion is replaced by Cs⁺ to form the CsPbI₃ structure. A series of spectroscopic measurements were performed to understand the crystal structure of MAPbI₃ with Cs⁺ incorporation. X-ray energy dispersive spectroscopy (EDS) measurements are used to estimate the Cs⁺ content inside the lattice of perovskite by the three model approximation which is reported in our earlier publication.¹¹

We prepared standalone MAPbI₃ films on glass using a two step halide perovskite fabrication approach; the details of the methods were reported earlier.¹¹ Cation exchange was performed at room temperature by dipping the MAPbI₃ film into an IPA-Cs solution with ionic Cs. The concentration of incorporated Cs into the MAPbI₃ was varied by changing the dipping time. This method was previously reported, and the prepared samples were well-characterized. The entire synthesis was performed inside a glovebox.

Scanning electron microscopy (SEM) images were acquired with a field-emission high-resolution scanning electron microscope (Helios 600, FEI). The energy-dispersive X-ray analysis

(EDAX) was performed on an 80 mm² large area SSD detector (X-Max, Oxford Instruments).

X-ray diffraction (XRD) measurements were performed on a Bragg–Brentano geometry X-ray diffractometer (D8, Bruker) (Cu Kα₁ with λ = 1.5406 Å and CuKα₂ with λ = 1.5443 Å; intensity ratio of 2). All diffractograms were corrected against FTO as an internal standard. Baseline removal was performed with FITYK 0.9.8.

Resonance Raman spectroscopy was performed on the samples with laser excitation at a wavelength of 532 nm, resonating with the absorption band edge of PbI₂ at 540 nm (LabRam HR, JY Horiba). The backscattered light is collected via an objective and collimated. The Rayleigh scattering peak is filtered using a high-performance long pass Raman edge filter that permitted collection of Raman shifts as close as 75 cm⁻¹ away from the laser excitation. The cleaned Raman signal was then spatially filtered by focusing it through a confocal pinhole and before it was sent into the high-resolution spectrometer. An exposure of 30 s and a threshold power of 5 μW are kept standard throughout the measurements. To address the degradation of perovskite due to burning upon laser illumination, the samples are sealed in an inert atmosphere.

LFRS measurements were carried using an integrated laser and volume holographic (VHG) filter system (ONDAX, XLF-MICRO 532 nm) with 50 mW of optical power at an excitation wavelength of λ_{ex} = 532 nm. The laser output was routed into a lab microscope, and the Raman signal was fiber-coupled into an imaging spectrometer (Princeton Instruments, SP-2500i) with an EM-CCD camera (Princeton Instruments, ProEM 16002). Acquisition times of 60 s were used, and the grating groove density of 1800 g/mm was selected. The measurements were carried out by first setting the focus to the top surface and then slightly lowering the focal plane into the depth of the sample to avoid edge effects. At least 3 different regions were measured for each sample. The spectral baselines were shifted for presentation purposes. The integration time for spectral collection was 60 s per acquisition. Each spectrum was recorded by accumulating 5 frames, yielding an overall integration time of 300 s. The Raman frequencies were calibrated using a silicon wafer. All experiments were conducted at room temperature (293 K).

Absorption measurements were recorded on thin films with a spectrophotometer (Cary, UV–vis–NIR). Thin film absorbance was measured on a home-built optical scanner, measuring total transmission, total reflection, and specular reflection with millimeter spatial resolution in a high-throughput fashion.¹¹ The PL measurements were performed in a fluorescence spectrophotometer (Eclipse, Cary) in a steady-state mode similar to that used for absorption spectroscopy.

The three model approximation calculations from the EDS measurements mentioned above yield incorporation percentages for MA_{1-x}Cs_xPbI₃ to be x = 0.05, 0.24, 0.33, 0.59, 0.60, 0.80 (please see Table S1 in the Supporting Information). The absorption spectra presented in Figure 1 show the expected sharp absorption edge at 850 nm for pure MAPbI₃ films; upon Cs⁺ incorporation, the steep absorption band edge exhibits a continuous change to shallow absorption at 850 nm. Simultaneously, a complementary absorption peak appears at 480 nm, which builds up with Cs incorporation and marks an incremental blue shift until 440 nm, which closely matches to the absorption edge of *δ*-CsPbI₃. However, PbI₂, with an absorption band at 540 nm, leaves no signature in the Cs⁺

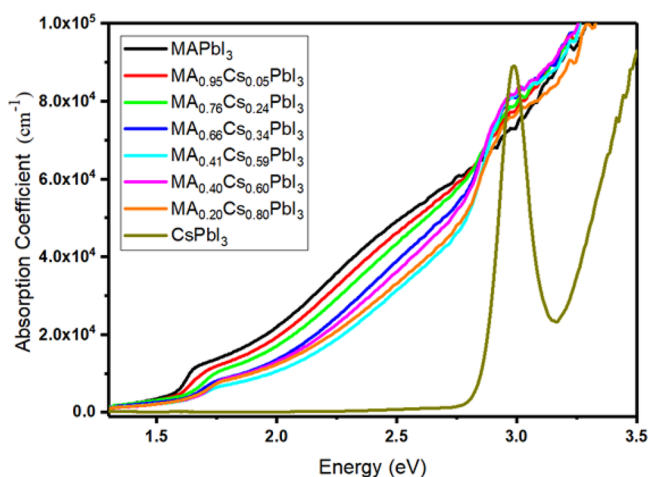


Figure 1. Absorption spectra of MAPbI₃, CsPbI₃, and Cs incorporated in an MAPbI₃ thin film with variation in the Cs concentration deposited on glass.

doped sample. It is known that the cubic phase of stabilized α -CsPbI₃ has two absorption bands at 730 and 440 nm, respectively.^{14,15} The experimental data follows the same trend, namely, that with Cs incorporation the sharp absorption edge at 750 nm shifts to a shallow absorption edge at 710 nm and with the appearance of an additional peak at 440 nm, indicating that optical properties of the final phase match to a greater extent those of stabilized α -CsPbI₃, and minimally to those of δ -CsPbI₃.

Figure 2 presents X-ray diffraction spectra of a pristine MAPbI₃ stand-alone film, MAPbI₃ with different Cs incorporation concentrations, and pristine CsPbI₃, PbI₂, and CsI in their respective order. The MAPbI₃ stand-alone film shows a high-intensity signature at $2\theta = 14.17^\circ$, corresponding to the (110) Bragg reflection plane. With an increase in Cs concentration, the (110) Bragg reflection plane shows an incremental shift to higher angles, i.e., 14.17 – 14.35° , and its intensity decreases, subsequently disappearing approximately at a Cs concentration of 0.80 and above. In the beginning of the Cs incorporation, at a concentration of 0.043, the Cs ion is accommodated in the lattice, without changing the structure of the hybrid perovskite. This results in a slight shift of the (110) Bragg plane from 14.17° to 14.20° , and this begins to shrink the lattice, marginally reducing the lattice constant. A continuous shift of the MAPbI₃ peak from 14.19° to 14.34° indicates reduction in d -spacing and, therefore, the unit volume. This is understood because of the smaller size of the Cs ion when compared to that of the methylamine ion. The XRD signature of CsPbI₃ is observed above a critical incorporation concentration of Cs = 0.24. This is evident by the appearance of diffraction peaks at 2θ values of 9.7° , 9.9° , 13.08° , 26.4° , 21.6° , 22.6° , 27.39° , and 28.9° at the concentration of 0.244, following which the intensity of these peaks increases with incorporation. Further, the peaks at 23.5° and 20.4° show a similar trend before disappearing at higher concentrations. The concentration of 0.59 exhibits a series of new peaks at 17.6° , 16.9° , 19.7° , 29.63° , and 30.6° . However, the concentration regime of 0.33–0.55 demonstrates a flip in the ratio of the peak intensities of 14.34° to 9.9° and 26.4° . This indicates the beginning of nucleation of a new crystal phase. The black phase of CsPbI₃ is assumed to exist between incorporation concentrations of 0.04–0.33. Further, for

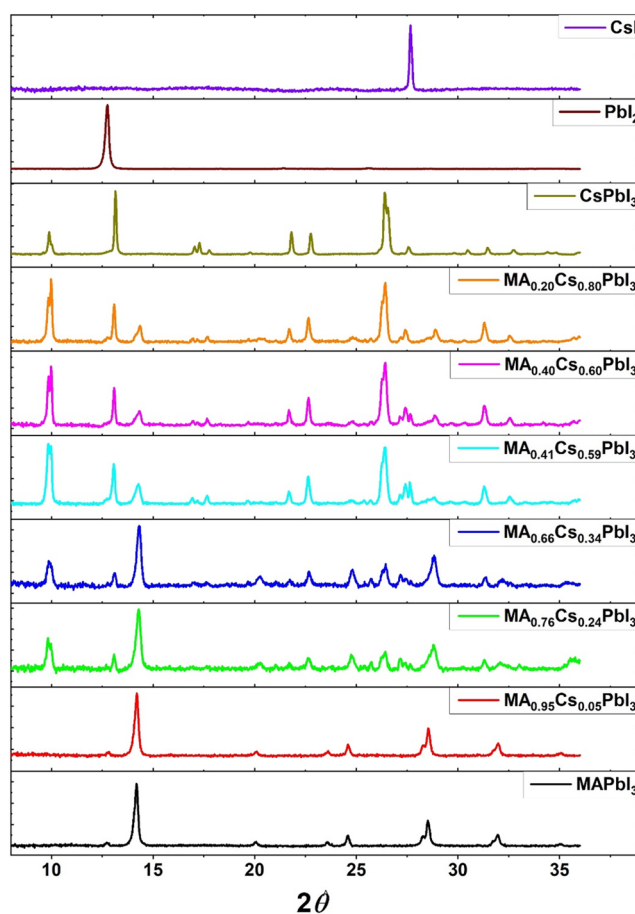


Figure 2. X-ray diffraction of MAPbI₃, CsPbI₃, and Cs incorporated in MAPbI₃ thin film with variation in the Cs concentration deposited on glass.

incorporation concentrations above 0.60, the δ phase of CsPbI₃ begins to form with a small proportion of stabilized α -CsPbI₃. Earlier studies explain the ion exchange process, in which MA is replaced by Cs in MAPbI₃.¹¹ At lower concentrations of Cs, it is assumed that Cs incorporation takes place interstitially, wherein Cs occupies interstitial sites. When the incorporation concentration exceeds the substitution limit of 0.13, Cs nucleates the formation of α -CsPbI₃. Further increases in concentration, upon crossing 0.59, nucleate δ -CsPbI₃. Thereafter, grain growth of both the phases occurs simultaneously at the expense of MAPbI₃. XRD spectroscopy further gives an insight into the mechanism of Cs incorporation. The strained structure of MAPbI₃, as compared to that of CsPbI₃, is favorable for an ion exchange reaction. The appearance of a nonstoichiometric composition of the MAPbI₃ surface is well-known.^{16,17} Therefore, I ions and MA ions are free toward any volatile ion escape processes leaving behind PbI₂, making the sites favorable for ion exchange. The traces of PbI₂, obtained at initial stages of Cs exchange until a concentration of 0.043, support this claim. Further, an initial appearance of the PbI₂ peak and the shift of the perovskite peak at 14.19° inform the ejection of an MA ion from the strained perovskite structure through the (001) plane acting as a channel for both ejection of the MA ion and intake of the Cs ion. With the ejection of the MA ion and intake of the Cs ion, the d -spacing of the (110) plane continuously shrinks. However, after reaching critical concentration, the Cs within

the MAPbI₃ crystals begins coagulation as a new CsPbI₃ grain adjacent to an MAPbI₃ grain. This results in formation of the stable α -CsPbI₃ phase, and after some time, β -CsPbI₃ is formed. The mixture of two different phases at the higher incorporation level of Cs ions implies this mechanism.

Raman spectra of MAPbI₃ and thin films of Cs incorporated MAPbI₃ were recorded with a scan window from 50 to 500 cm⁻¹ presented in Figure 3. It is observed that MAPbI₃ is very

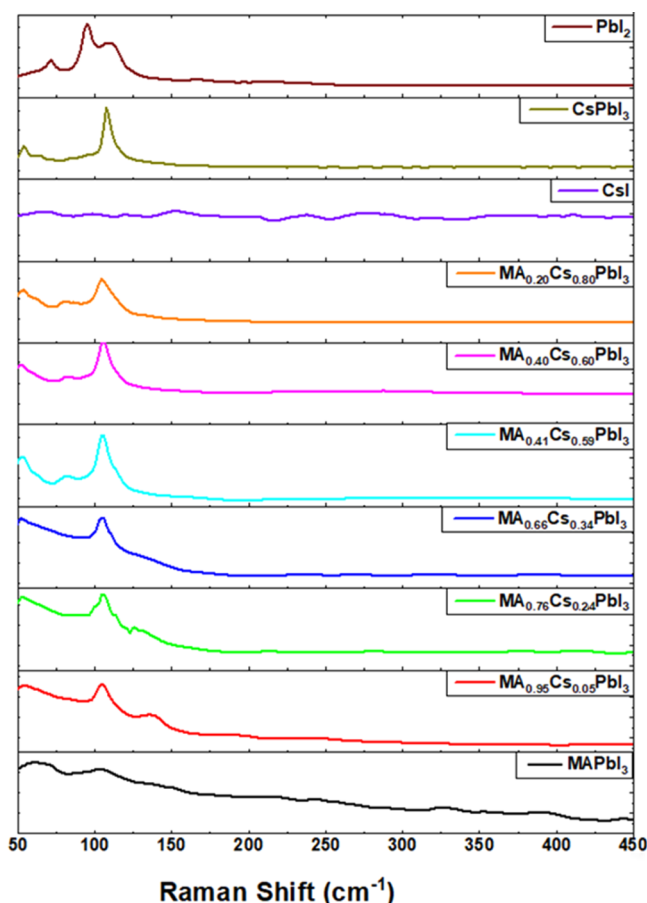


Figure 3. Resonance Raman spectra of MAPbI₃, PbI₂, CsPbI₃, CsI, and Cs incorporated MAPbI₃ thin film with variation in the Cs concentration deposited on glass.

sensitive to variation in power, and therefore, utmost care was required not to burn the samples. The peaks indicating burning of MAPbI₃ have been reported earlier¹⁸ at 94 and 220 cm⁻¹, and we did not observe these peaks in our measurement. Upon successive repeated trials at the same spot as well as in the vicinity of a pre-excited spot, no observable burning effect was detected in our measurements. Measuring the Raman signal with a number of repetitions at the same region, with laser powers held below 5 μ W, we neither observe any time evolution of Raman peaks nor see any third-order nonlinear effect that can yield an increase in the bandgap of the perovskite.

Cs incorporated MAPbI₃ films were subjected to Raman spectroscopy with PbI₂, CsI, and yellow phase CsPbI₃ as references. PbI₂ was observed to have Raman peaks at 72, 95, and 110 cm⁻¹, and yellow phase CsPbI₃ was observed to have peaks at 53 and 107 cm⁻¹, whereas CsI did not show any Raman vibrational modes. Further, the MAPbI₃ film showed peaks at 64 and 107 cm⁻¹, consistent with earlier reports.^{19,20}

The dipole nature of the MA cation influences the long-range alignment of the ordered structure in MAPbI₃. The vibrational modes of the PbI₆ octahedral cage is observed below 250 cm⁻¹. The symmetric stretching of modes of this octahedral cage is expected at \sim 107 cm⁻¹ followed by an asymmetric deformation at 64 cm⁻¹, reported earlier.^{18,21,22} In general, peaks at 64 and 107 cm⁻¹ are assigned to the PbI₃ vibrational modes and cage distortion, respectively, and asymmetric stretching and bending of Pb–I are observed between 40 and 90 cm⁻¹. Peaks between 140 and 400 cm⁻¹ are assigned to stretching, wagging, and MA–MA asymmetrical stretching modes. The broad peaks at 250 and 390 cm⁻¹ are assigned to be torsional modes of MA ions, and those at 100–200 cm⁻¹ are purely associated with the liberation of the MA cation. Thus, the peak at 138 cm⁻¹ is assigned similarly.^{23,24} Organic molecules have several additional degrees of rotational and torsional freedom. These degrees of freedom result in various modes of vibration, causing disorder in the system. Here, the torsional mode is directly connected to the interaction between the motion of the cation and cage.²³

MAPbI₃ at room temperature is tetragonal in structure showing two broad unresolved peaks at 64 and 107 cm⁻¹. In addition to these peaks, we observe a broad spectrum from 110 to 250 cm⁻¹, which includes an unresolvable librational mode at 140 cm⁻¹ and a torsional mode at 240 cm⁻¹. The absence of strong band filling of Raman peaks can be attributed to a lack of rigidity and enormous disorder in the cage structure which is induced by strong coupling between Pb–I and MA⁺ ions.

Incorporation of Cs ion brings rigidity to the structure because of the change in ionic size of the Cs ion. The Raman spectrum of the Cs incorporated MAPbI₃ ($x = 0.04$) sample shows distinct new features in the spectrum. The peak at 64 cm⁻¹ is shifted to 53.8 cm⁻¹, and an additional peak appears at 136 cm⁻¹. The peaks sharpen, indicating the hindrance for the MA liberation, which could also be because of torsion modes. There is a considerable decrease in the broad stretched peak from 150 to 450 cm⁻¹ due to shrinking the unit cell upon Cs incorporation and to deforming the octahedral structure. The strengthening of the bond vibrational frequency and reduction in the liberation frequency could be a reason for the appearance of an additional peak at 140 cm⁻¹. Further, Cs incorporation ($x = 0.24$) continuously blue-shifts the 52.5 cm⁻¹ peak, and the main peaks become sharper and more well-separated. The new peak observed at 136 cm⁻¹ is blue-shifted to 125.7 cm⁻¹, indicating a continuous tilt of the PbI₂ octahedral frame and lattice shrinking. The incremental incorporation of Cs ($x = 0.34$) further blue-shifts the band at 52.5–51.8 cm⁻¹, and the 104 cm⁻¹ peak becomes narrower with an increase in intensity. The peak at 125 cm⁻¹, at this incorporation concentration, is reduced to a broad shoulder from 120 to 130 cm⁻¹, and the torsional and liberation modes disappear completely. The Raman spectrum at Cs incorporation levels of $x = 0.55$ shows an additional peak at 81.3 cm⁻¹. This additional peak indicates a new phonon mode being active, which could be a result of the coexistence of α -CsPbI₃ and β -CsPbI₃. This mode continues to evolve and splits into two different vibrational modes, 80.6 and 86.0 cm⁻¹.

At room temperature, MAPbI₃ exists in the tetragonal structure with enormous dynamic disorder. At higher temperatures, it undergoes a phase transition to cubic and at lower temperatures to orthorhombic structures. Using specialized notch filters (ultranarrow laser line filter) in the Raman measurement system, which allow measurements of both

Stokes and anti-Stokes shifts in the same scan window, and using high-resolution gratings, we have recorded highly resolved LFRS peaks. So far, all the reported LFRS modes for OHP are recorded at low temperature.²⁵ However, intriguingly, we observe the LFRS modes for OHP at room temperature. We present here evolution of LFRS for both CsPbI₃ and Cs incorporated into MAPbI₃ shown in Figure 4.

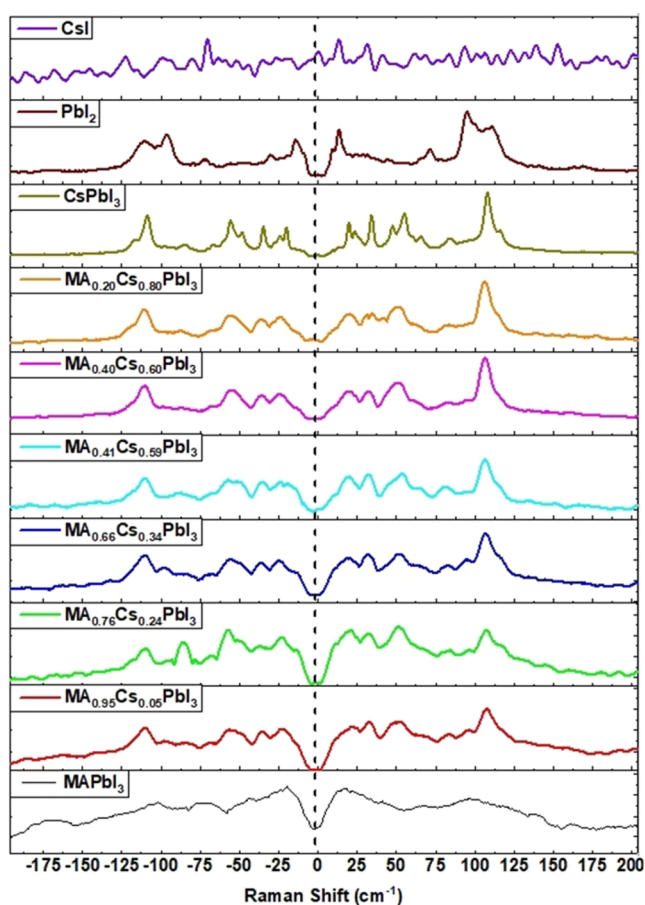


Figure 4. Low-frequency Raman spectra of MAPbI₃, PbI₂, CsPbI₃, CsI, and Cs incorporated in an MAPbI₃ thin film with variation in the Cs concentration deposited on glass.

Our main observations include broadening of Raman frequencies near excitation upon Cs incorporation. The broad distribution of the central peak in LFRS is due to isotopic disorder which is induced by MA ion rotation.^{26,27} With Cs incorporation, the central peak becomes wider and almost aligned with the baseline, in addition to which all LFRS peaks become sharper and better resolved. These changes indicate a suppression of the anharmonic motion of the cations in the halide perovskite and local polar phonon fluctuation of the perovskite structure. Further, it can be seen that Cs incorporation induces many sharp vibrational modes in the MAPbI₃. Typically, the anharmonic motion of MA cations causes giant disorder in the crystal, and this is damped by the Cs ions which add long-range ordering in the crystal structure. Moreover, all the LFRS peaks match with the reported Raman peaks for CsPbBr₃ from α cubic and δ orthorhombic structure.^{25,28} It appears that a small percentage of Cs incorporation is enough to decrease anharmonic motion of the MA ions and the interaction of the cage, ultimately enhancing all Raman active modes. Further, it is seen that pure

PbI₂ films have LFRS peaks at 10, 13, 17, 94, and 110 cm⁻¹, whereas the tetragonal structure of MAPbI₃ has two broad peaks at 64 and 107 cm⁻¹. In addition, LFRS measurements of the pristine CsPbI₃ have peaks at 19, 23, 34, 47, 55, 66, 84, 108, and 115 cm⁻¹. It is observed that MAPbI₃ has broad shoulder-like peaks near the excitation which mask the LF vibration modes of perovskite. This is due to isotopic disorder and intrinsic local polar fluctuations of MA cations. Upon Cs incorporation, LFRS peaks for perovskites are observed at 19, 32, 50, 83, 95, and 110 cm⁻¹, which are of distorted tetragonal structure, close to the reported peaks for the orthorhombic structure of CsPbBr₃ at low temperature.²⁵ With an increase in the Cs concentration in MAPbI₃, all peaks except those at 83 and 95 cm⁻¹ are observed to be strongly enhanced, which closely matches with the LFRS of δ -CsPbI₃. It is reported that peaks at 19 and 32 cm⁻¹ are related to the vibration and complex motions of the "A" cation, whereas peaks that appeared at 50 and 83 cm⁻¹ arise from the vibrations of the Pb–I bond, which witnesses a strong coupling with the center A ion.^{25,29,30}

The observed LFRS peaks at 19, 32, 50, and 83 cm⁻¹ for Cs incorporated samples indicate a mixture of α -CsPbI₃ and tetragonal MAPbI₃. The increase in Cs incorporation results in structural evolution, yielding a mixed phase of α -CsPbI₃ and δ -CsPbI₃. More importantly, spectral widening near the excitation laser and, upon Cs incorporation, sharpening of all Raman modes indicate a transformation from the disordered structure of MAPbI₃ to a more rigid and ordered structure.

The PL spectra presented in Figure 5 show appreciable blue shifts in peak position with Cs incorporation. The excitation

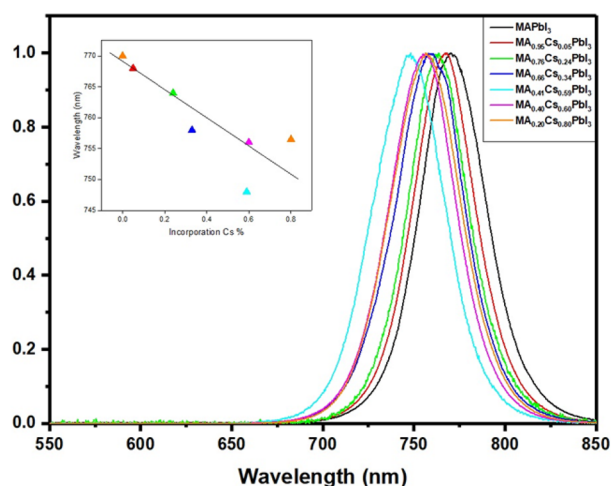


Figure 5. PL spectra of MAPbI₃ and Cs doped MAPbI₃ thin film with variation in the Cs incorporation concentration deposited on glass. Inset is the graphical representation of variation of the PL peak with Cs ion concentration.

occurs mainly at the Pb–I bond in the MAPbI₃, which has PL at 770 nm. Upon Cs incorporation, the PL is observed to shift to lower wavelengths due to shrinking of sublattice and strengthening of the Pb–I bond. The PL observed after a series of Cs incorporation is mainly due to the excitation of α -CsPbI₃, since δ -CsPbI₃ is a wide bandgap material.¹⁵

In summary, we have demonstrated the structural evolution of tetragonal MAPbI₃ through the Cs ion exchange process in freestanding films from α -CsPbI₃ to δ -CsPbI₃. The absorption and XRD measurements confirmed the formation of stabilized

α -CsPbI₃. Sudden phase changes are witnessed when the concentration fraction of Cs in MAPbI₃ is in the range of $x = 0.2$ – 0.59 , due to nucleation of stable δ -CsPbI₃. Resonance Raman and LFRS spectra of the perovskite suggest reduction in both anharmonic oscillation and thermal fluctuation in MAPbI₃ upon Cs incorporation, in addition to enhanced rigidity and long-range order in MAPbI₃ structure. This observation explains the previously reported prolonged increase in the stability of the hybrid perovskite upon Cs incorporation. Therefore, this remarkable increase in stability for Cs incorporated MAPbI₃ is attributed to an increase in rigidity and induced order in the structure. Further, reduction in the thermal fluctuations contributes to improving the stability of the hybrid perovskites.

■ ASSOCIATED CONTENT

Supporting Information

The Supporting Information is available free of charge on the ACS Publications website at DOI: 10.1021/acsaem.8b01539.

EDAX calculations (PDF)

■ AUTHOR INFORMATION

Corresponding Author

*E-mail: Yaakov.Tischler@biu.ac.il.

ORCID

Vinayaka H. Damle: 0000-0001-9670-064X

Laxman Gouda: 0000-0001-9022-0151

Yaakov R. Tischler: 0000-0001-8016-538X

Author Contributions

[†]V.H.D. and L.G. have contributed equally to this work.

Notes

The authors declare no competing financial interest.

■ ACKNOWLEDGMENTS

We would like to thank Dr. Anjani Nagvenkar for helping us with EDAX measurements, Prof. Arie Zaban and Prof. David Cahen for laboratory space for perovskite fabrication, and Dr. Basanth S. Kalanoor for fruitful discussion. V.H.D. greatly acknowledges Bar-Ilan University for supporting his research through the President's Scholarship Program.

■ REFERENCES

- (1) Kojima, A.; Teshima, K.; Shirai, Y.; Miyasaka, T. Organometal Halide Perovskites as Visible-Light Sensitizers for Photovoltaic Cells. *J. Am. Chem. Soc.* **2009**, *131*, 6050–6051.
- (2) Amat, A.; Mosconi, E.; Ronca, E.; Quarti, C.; Umari, P.; Nazeeruddin, M. K.; Grätzel, M.; De Angelis, F. Cation-Induced Band-Gap Tuning in Organohalide Perovskites: Interplay of Spin-Orbit Coupling and Octahedra Tilting. *Nano Lett.* **2014**, *14*, 3608–3616.
- (3) Yaffe, O.; Guo, Y.; Tan, L. Z.; Egger, D. A.; Hull, T.; Stoumpos, C. C.; Zheng, F.; Heinz, T. F.; Kronik, L.; Kanatzidis, M. G.; Owen, J. S.; Rappe, A. M.; Pimenta, M. A.; Brus, L. E. Local Polar Fluctuations in Lead Halide Perovskite Crystals. *Phys. Rev. Lett.* **2017**, *118*, 136001.
- (4) Wang, Q.; Lyu, M.; Zhang, M.; Yun, J. H.; Chen, H.; Wang, L. Transition from the Tetragonal to Cubic Phase of Organohalide Perovskite: The Role of Chlorine in Crystal Formation of CH₃NH₃PbI₃ on TiO₂ Substrates. *J. Phys. Chem. Lett.* **2015**, *6*, 4379–4384.
- (5) Chen, J.; Zhou, S.; Jin, S.; Li, H.; Zhai, T. Crystal Organometal Halide Perovskites with Promising Optoelectronic Applications. *J. Mater. Chem. C* **2016**, *4*, 11.

- (6) Niu, G.; Guo, X.; Wang, L. Review of Recent Progress in Chemical Stability of Perovskite Solar Cells. *J. Mater. Chem. A* **2015**, *3*, 8970–8980.

- (7) Gottesman, R.; Gouda, L.; Kalanoor, B. S.; Haltzi, E.; Tirosh, S.; Rosh-Hodesh, E.; Tischler, Y.; Zaban, A.; Quarti, C.; Mosconi, E.; De Angelis, F. Photoinduced Reversible Structural Transformations in Free-Standing CH₃NH₃PbI₃ Perovskite Films. *J. Phys. Chem. Lett.* **2015**, *6*, 2332–2338.

- (8) Zarick, H. F.; Soetan, N.; Erwin, W. R.; Bardhan, R. Mixed Halide Hybrid Perovskites: A Paradigm Shift in Photovoltaics. *J. Mater. Chem. A* **2018**, *6*, 5507.

- (9) Niu, G.; Li, W.; Li, J.; Liang, X.; Wang, L. Enhancement of Thermal Stability for Perovskite Solar Cells through Cesium Doping. *RSC Adv.* **2017**, *7*, 17473–17479.

- (10) Ma, X. X.; Li, Z. S. Substituting Cs for MA on the Surface of MAPbI₃ Perovskite: A First-Principles Study. *Comput. Mater. Sci.* **2018**, *150*, 411–417.

- (11) Niemann, R. G.; Gouda, L.; Hu, J.; Tirosh, S.; Gottesman, R.; Cameron, P. J.; Zaban, A. Cs⁺ Incorporation into CH₃NH₃PbI₃ Perovskite: Substitution Limit and Stability Enhancement. *J. Mater. Chem. A* **2016**, *4*, 17819–17827.

- (12) Harwell, J. R.; Payne, J. L.; Sajjad, M. T.; Heutz, F. J. L.; Dawson, D. M.; Whitfield, P. S.; Irvine, J. T. S.; Samuel, I. D. W.; Carpenter, M. A. Role of lattice distortion and A site cation in the phase transitions of methylammonium lead halide perovskites. *Phys. Rev. Materials* **2018**, *2*, 065404.

- (13) Matsuo, H.; Noguchi, Y.; Miyayama, M. Gap-State Engineering of Visible-Light-Active Ferroelectrics for Photovoltaic Applications. *Nat. Commun.* **2017**, *8*, 207.

- (14) Kato, M.; Fujiseki, T.; Miyadera, T.; Sugita, T.; Fujimoto, S.; Tamakoshi, M.; Chikamatsu, M.; Fujiwara, H. Universal Rules for Visible-Light Absorption in Hybrid Perovskite Materials. *J. Appl. Phys.* **2017**, *121*, 115501.

- (15) Wang, Q.; Zheng, X.; Deng, Y.; Zhao, J.; Chen, Z.; Huang, J. Stabilizing the α -Phase of CsPbI₃ Perovskite by Sulfobetaine Zwitterions in One-Step Spin-Coating Films. *Joule* **2017**, *1*, 371–382.

- (16) Ono, L. K.; Qi, Y. Surface and Interface Aspects of Organometal Halide Perovskite Materials and Solar Cells. *J. Phys. Chem. Lett.* **2016**, *7*, 4764–4794.

- (17) Guo, X.; McCleese, C.; Lin, W.-C.; Burda, C. Curing of Degraded MAPbI₃ Perovskite Films. *RSC Adv.* **2016**, *6*, 60620–60625.

- (18) Ledinský, M.; Löper, P.; Niesen, B.; Holovský, J.; Moon, S. J.; Yum, J. H.; De Wolf, S.; Fejfar, A.; Ballif, C. Raman Spectroscopy of Organic-Inorganic Halide Perovskites. *J. Phys. Chem. Lett.* **2015**, *6*, 401–406.

- (19) Park, B. W.; Jain, S. M.; Zhang, X.; Hagfeldt, A.; Boschloo, G.; Edvinsson, T. Resonance Raman and Excitation Energy Dependent Charge Transfer Mechanism in Halide-Substituted Hybrid Perovskite Solar Cells. *ACS Nano* **2015**, *9*, 2088–2101.

- (20) Pistor, P.; Ruiz, A.; Cabot, A.; Izquierdo-Roca, V. Advanced Raman Spectroscopy of Methylammonium Lead Iodide: Development of a Non-Destructive Characterisation Methodology. *Sci. Rep.* **2016**, *6*, 35973.

- (21) Quarti, C.; Grancini, G.; Mosconi, E.; Bruno, P.; Ball, J. M.; Lee, M. M.; Snaith, H. J.; Petrozza, A.; De Angelis, F. The Raman Spectrum of the CH₃NH₃PbI₃ Hybrid Perovskite: Interplay of Theory and Experiment. *J. Phys. Chem. Lett.* **2014**, *5*, 279–284.

- (22) Yaffe, O.; Guo, Y.; Tan, L. Z.; Egger, D. A.; Hull, T.; Stoumpos, C. C.; Zheng, F.; Heinz, T. F.; Kronik, L.; Kanatzidis, M. G.; Owen, J. S.; Rappe, A. M.; Pimenta, M. A.; Brus, L. E. Local Polar Fluctuations in Lead Halide Perovskite Crystals. *Phys. Rev. Lett.* **2017**, *118*, 136001.

- (23) Niemann, R. G.; Kontos, A. G.; Palles, D.; Kamitsos, E. I.; Kaltzoglou, A.; Brivio, F.; Falaras, P.; Cameron, P. J. Halogen Effects on Ordering and Bonding of CH₃NH₃ in CH₃NH₃PbX₃ (X = Cl, Br, I) Hybrid Perovskites: A Vibrational Spectroscopic Study. *J. Phys. Chem. C* **2016**, *120*, 2509–2519.

- (24) Leguy, A. M. A.; Goñi, A. R.; Frost, J. M.; Skelton, J.; Weber, O. J.; Pallipurath, A.; Alonso, M. I.; Campoy-Quiles, M.; Weller, M. T.;

et al. Dynamic Disorder, Phonon Lifetimes, and the Assignment of Modes to the Vibrational Spectra of Methylammonium Lead Halide Perovskites. *Phys. Chem. Chem. Phys.* **2016**, *18*, 27051–27066.

(25) Guo, Y.; Yaffe, O.; Paley, D. W.; Beecher, A. N.; Hull, T. D.; Szpak, G.; Owen, J. S.; Brus, L. E.; Pimenta, M. A. Interplay between Organic Cations and Inorganic Framework and Incommensurability in Hybrid Lead-Halide Perovskite CH₃NH₃PbBr₃. *Phys. Rev. Mater.* **2017**, *1*, 042041.

(26) Weller, M. T.; Weber, O. J.; Henry, P. F.; Di Pumpo, A. M.; Hansen, T. C. Complete Structure and Cation Orientation in the Perovskite Photovoltaic Methylammonium Lead Iodide between 100 and 352 K. *Chem. Commun.* **2015**, *51*, 4180–4183.

(27) Gong, J.; Yang, M.; Ma, X.; Schaller, R. D.; Liu, G.; Kong, L.; Yang, Y.; Beard, M. C.; Lesslie, M.; Dai, Y.; Huang, B.; Zhu, K.; Xu, T. Electron-Rotor Interaction in Organic-Inorganic Lead Iodide Perovskites Discovered by Isotope Effects. *J. Phys. Chem. Lett.* **2016**, *7*, 2879–2887.

(28) Miyata, K.; Atallah, T. L.; Zhu, X. Y. Lead Halide Perovskites: Crystal-Liquid Duality, Phonon Glass Electron Crystals, and Large Polaron Formation. *Sci. Adv.* **2017**, *3*, e1701469.

(29) Brivio, F.; Frost, J. M.; Skelton, J. M.; Jackson, A. J.; Weber, O. J.; Weller, M. T.; Goñi, A. R.; Leguy, A. M. A.; Barnes, P. R. F.; Walsh, A. Lattice Dynamics and Vibrational Spectra of the Orthorhombic, Tetragonal, and Cubic Phases of Methylammonium Lead Iodide. *Phys. Rev. B: Condens. Matter Mater. Phys.* **2015**, *92*, 144308–8.

(30) Ahmed, T.; La-O-Vorakiat, C.; Salim, T.; Lam, Y. M.; Chia, E. E. M.; Zhu, J. X. Optical Properties of Organometallic Perovskite: An Ab Initio Study Using Relativistic GW Correction and Bethe-Salpeter Equation. *EPL* **2014**, *108*, 67015.